REPORT DOCUMENTATION PAGE

1a. REPORT SECURITY CLASSIFICATION UNCLASSIFIED	1b. RESTRICTIVE MARKINGS
2a. SECURITY CLASSIFICATION AUTHORITY	3. DISTRIBUTION / AVAILABILITY OF REPORT Approved for public release; distribution is unlimited.
2b. DECLASSIFICATION / DOWNGRADING SCHEDULE	
4. PERFORMING ORGANIZATION REPORT NUMBER(S) TR 8089	5. MONITORING ORGANIZATION REPORT NUMBER(S)
6a. NAME OF PERFORMING ORGANIZATION Naval Underwater Systems Center 6b. OFFICE SYMBOL (If applicable)	7a. NAME OF MONITORING ORGANIZATION
6c. ADDRESS (City, State, and ZIP Code) New London Laboratory New London, CT 06320	7b. ADDRESS (City, State, and ZIP Code)
8a. NAME OF FUNDING / SPONSORING ORGANIZATION 8b. OFFICE SYMBOL (If applicable)	9. PROCUREMENT INSTRUMENT IDENTIFICATION NUMBER
8c. ADDRESS (City, State, and ZIP Code)	10. SOURCE OF FUNDING NUMBERS PROGRAM ELEMENT NO. / PROJECT NO. / TASK NO. / WORK UNIT ACCESSION NO.
11. TITLE (Include Security Classification) ARCTIC ICE ATTENUATION MODEL STUDY: FINAL REPORT	
12. PERSONAL AUTHOR(S) Dr. R. H. Mellen, OMNI Analysis, and LT. P. M. Scheifele, NUSC, NLLAB	
13a. TYPE OF REPORT 13b. TIME COVERED FROM _____ TO _____	14. DATE OF REPORT (Year, Month, Day) 1987 September 1 15. PAGE COUNT
16. SUPPLEMENTARY NOTATION	

17. COSATI CODES		
FIELD	GROUP	SUB-GROUP

18. SUBJECT TERMS (Continue on reverse if necessary and identify by block number)
Ice
Arctic
Attenuation

19. ABSTRACT (Continue on reverse if necessary and identify by block number)

Underwater acoustic propagation in the Arctic Ocean is characterized by a refractive surface-channel with a rough boundary. Scattering estimates based on free-surface theory have proven low by more than a factor of two in forward-scatter loss and low by 20 dB or more in backscatter strength. Failure to account for either attenuation or backscattering indicates that impedance effects must be involved. The ice layer is modeled as a uniform elastic solid. Perturbation analysis shows scattering from slopes as well as displacements. Displacements produce piston-like rereradiation in addition to the usual vertical-dipole type associated with free surfaces. The "rocking" horizontal dipole produced by slopes is evidently a significant mechanism at the lower frequencies. However, estimates of both attenuation and backscatter strength are much too low compared with experimental data.

20. DISTRIBUTION / AVAILABILITY OF ABSTRACT ☒ UNCLASSIFIED/UNLIMITED ☐ SAME AS RPT. ☐ DTIC USERS	21. ABSTRACT SECURITY CLASSIFICATION UNCLASSIFIED
22a. NAME OF RESPONSIBLE INDIVIDUAL LT. P. M. Scheifele	22b. TELEPHONE (Include Area Code) (203) 440-6589 22c. OFFICE SYMBOL Code 60

NUSC Technical Report 8089
1 September 1987

Arctic Ice Attenuation Model Study: Final Report

R. H. Mellen
OMNI Analysis

P. M. Scheifele
Combat Systems Analysis Staff

Naval Underwater Systems Center
Newport, Rhode Island / New London, Connecticut

Preface

This report was prepared for the Naval Underwater Systems Center, Principal Investigator LT P. M. Scheifele, Code 61M. The report was prepared by Dr. R. H. Mellen, OMNI Analysis, and co-authored by LT. P. M. Scheifele of the Naval Underwater Systems Center, New London Laboratory.

The authors wish to acknowledge J. Keil, E. Jensen, and J. Cohen for their guidance and support during the preparation of this report.

Reviewed and Approved: 1 September 1987

J. G. Keil
Head, Combat Systems Analysis Department

ARCTIC ICE ATTENUATION MODEL STUDY

FINAL REPORT

Submitted by:

Dr. R. H. Mellen
OMNI ANALYSIS
106 Boston Post Rd.
Waterford CT 06385
August 1987

Prepared under
NUSC Contract*N66604-87-D-0090
for:

Code 3332, E. Jensen (COTR)
Code 61, Lt. P.S. Scheifele (PI)

U. S. Naval Underwater Systems Center
New London Laboratory
New London, CT 06320

TABLE OF CONTENTS page

Summary

Low-frequency attenuation in the Arctic Ocean is more than an order of magnitude greater than that in the open ocean. Scattering at the ice/water interface is the most likely mechanism. Earlier estimates, based on Marsh theory for sea-surface scattering, showed reasonable consistency with experiment. However, analysis of more recent experiments, with roughness parameters derived from concurrent measurement of the underice profiles, yields values that are low by more than a factor of two.

The approximations of Marsh theory have been investigated. More exact calculation of the scattering integral by numerical methods has been found to increase the discrepency at low frequencies.

Failure of the pressure-release approximation to account for attenuation suggests that impedance effects are involved. For impedance calculations, the ice layer is modeled as a uniform elastic solid, assuming that acoustic contact at the ice/water interface is perfect. Trapped air could reduce the effective impedance, making the pressure-release assumption valid. The transfer function of acoustic pressure to vertical velocity is estimated by comparing hydrophone and seismometer signals and no evidence of such an impedance discontinuity is found. However, horizontal surface velocities are much greater than predicted by thin-plate theory, which supports a "rocking" motion produced by slopes.

Perturbation analysis shows scatter by both the vertical displacements and the slopes of the ice/water interface. The displacements produce a vertical velocity-dipole component of scatter in addition to a vertical pressure-dipole component analogous to the free-surface case. The latter is the dominant mechanism at higher frequencies while the former is negligible. The horizontal-dipole component produced by slopes may be a significant mechanism at low frequencies; however, the predicted values of scattering loss still fall far short of agreement with data.

Introduction

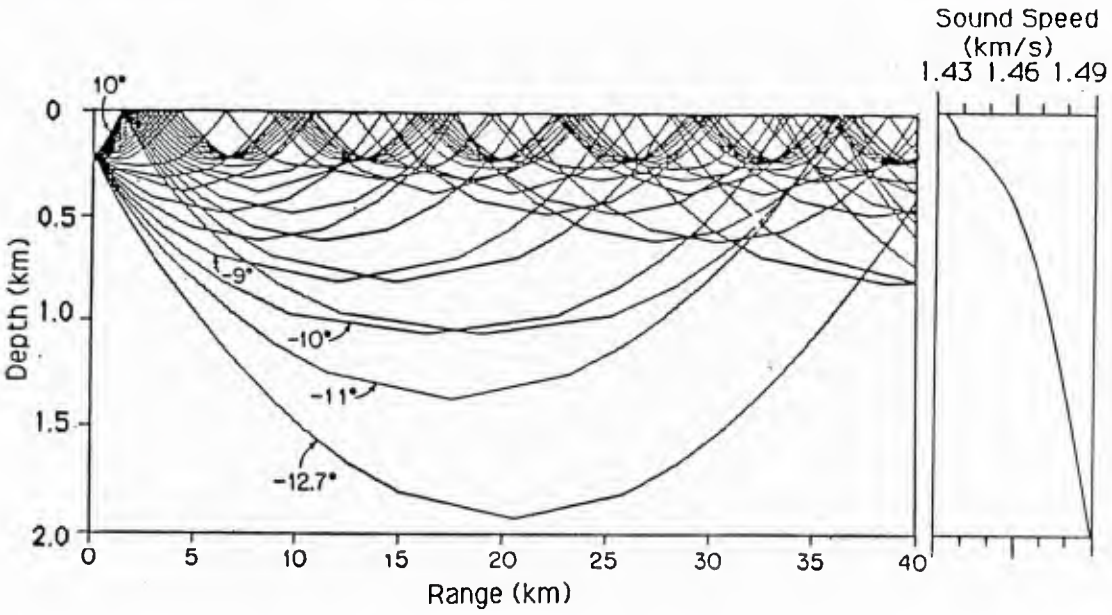

Figure 1: Arctic Ocean sound-speed profile and ray diagram.

The Arctic Ocean is a unique acoustic environment, principally because the sound speed increases monotonically with depth and the surface is usually covered by ice. Upward refraction coupled with the effects of the rough ice/water interface cause severe reverberation and attenuation, both of which can limit SONAR performance.

Figure 1 shows a typical sound-speed profile and ray diagram. In deeper waters, the maximum RSR cycle distance is of the order of 50 km. At short range, reverberation and absorption in the medium are the limiting factors. At long ranges, most of the energy is concentrated at low grazing angles. Multiple reflections at the ice/water interface are then involved and the resulting loss can exceed absorption by more than an order of magnitude.

The suspected mechanism is scattering at the rough ice/water interface. Early modeling efforts were based on the sea-surface theory of Marsh [1]. Free-surface theory appeared to give plausible results; i.e. the predictions were consistent with experiment for the standard deviation 2.3m, a value in reasonable agreement with underice-profile data.

Marsh theory is valid only over a limited range of angle and frequency. Recent advances in scattering theory now permit numerical calculation over a wider domain. In addition to improved theory, data are available from underice profiles taken concurrently with propagation measurements. With more reliable estimates of standard deviation and correlation length, the calculated scattering losses for the free-surface approximation are consistently low by more than a factor of two.

In earlier work, the ice/water interface was taken as compliant mainly because theory for finite-impedance boundaries was not available. Theory for a rough fluid/solid interface still does not exist. To approximate the effects of acoustic impedance, we consider a uniform flat elastic layer and treat roughness by the perturbation method. Impedance is calculated by the theory of Brekhovskikh [2].

In the compliant case, displacements reradiate as vertical-dipoles. At low frequencies and grazing angles, ice impedance tends to mass-loading and the elastic effects vanish. Ice floats on water and is isostatic on the average, the total mass being equal to that of the displaced water. In this limit, the layer would become quite transparent. However, if isostacy does not occur on the scales involved, some vertical-dipole scattering can be expected since the ice/water density ratio is roughly 0.9.

Although the roughness of the air/ice interface can also have an effect, the magnitudes are small because standard deviations are small compared to the ice/water interface.

Losses due to dissipation within the layer also appear to be small except at high frequencies and grazing angles where resonance occurs between the acoustic wave in water and the shear or compressional waves in ice. For the low frequencies and grazing angles involved in Arctic propagation, dissipation should be negligible.

Impedance effects could become negligible if acoustic coupling at the ice/water interface were reduced by trapped air. Comparison of vertical-seismometer and hydrophone signals shows no indication of this type of impedance discontinuity. However, the horizontal-seismometer signals are much greater than predicted by flat-plate theory, indicating that slopes are also involved in the ice motion in response to acoustic waves.

The perturbation method does not consider local grazing-angle effects. Finite slopes increase the "effective" grazing-angle, which also increases acoustic coupling at rough solid boundaries. Schmidt and Kuperman [3] have considered this problem; however, their analysis is based on the Kirchhoff (tangent-plane) method, which is valid only at higher frequencies.

At finite-impedance boundaries, the slopes produce a horizontal-dipole component of radiation associated with "rocking" motion. Analysis shows that this is a significant scattering mechanism at the lower frequencies. However, attenuation calculations still fall far short of agreement with experimental data in this range.

The purpose of this report is to review the experimental and theoretical evidence, in the hope that resolution of the remaining questions will lead to an accurate predictive model.

Attenuation data

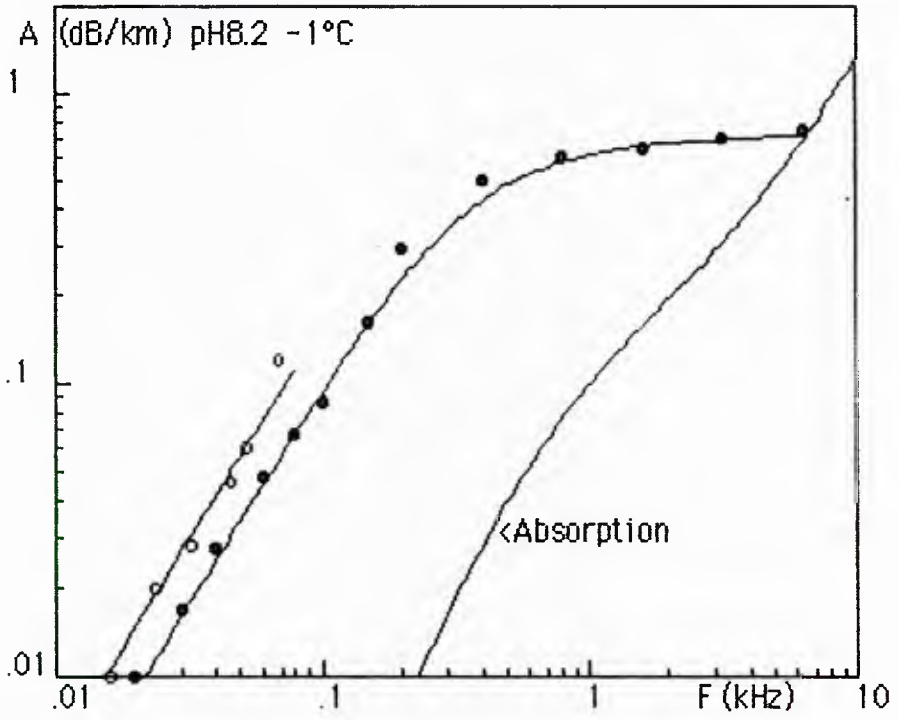

Figure 2: Arctic attenuation measurements.

Figure 2 compares attenuation data with predicted absorption in Arctic sea-water. The solid circles are 1959 NUSC data [4] and open circles are Tristen/Fram-82 data [5]. The connecting curves are arbitrary.

The striking features of the data are the magnitude and resemblence to relaxational phenomena. Below 1 kHz, the values are more than 10 times greater than absorption. Saturation at high frequencies is believed to be due, in part, to experimental conditions. At high frequencies, attenuation limits the useable range to less than 50 km and absorption dominates in this régime. At low frequencies, long ranges are required in order to make accurate measurements and ice loss then becomes dominant.

The likely mechanism is scattering at the rough ice/water interface. The theory for free-surface scattering shows that the reflection loss depends linearly on grazing angle for small angles. Since skip distance has similar dependence, loss vs range depends mainly on gradient. Ray angles greater than about 8° encounter a smaller gradient; however, divergence effects are greater and contributions are small at long ranges. Cutoff by bottom topography may be an important factor.

We next examine the statistical model of underice roughness to be used in calculating reflection loss.

Ice Model

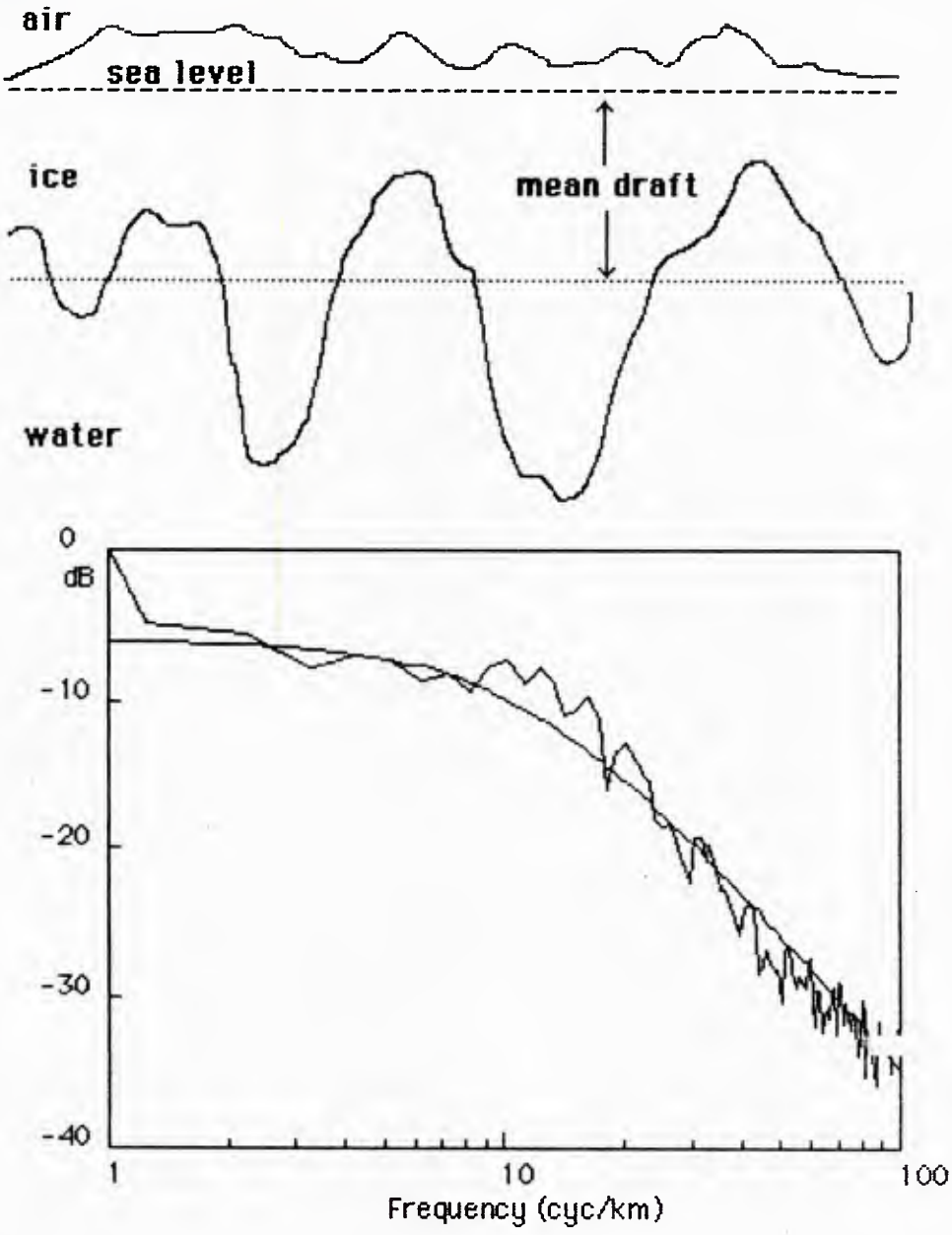

1-Dimensional Spectrum $S_1 = h^2\Omega_0^2/(\Omega_0^2+\Omega^2)^{3/2}$
Correlation Function $\Psi = h^2(\Omega_0 r)K_1(\Omega_0 r)$
2-Dimensional Spectrum $S_2 = 2h^2\Omega_0^2/(\Omega_0^2+\Omega^2)^2$
Standard Deviation RMS h=2m
Correlation Length $L=2/\Omega_0$ =44m

Figure 3: Ice roughness spectrum model.

Figure 3 shows a sketch of a typical ice profile. The graph is a spectrum of the ice/water interface roughness (Air/ice interface roughness is small and will be neglected). The analytic spectrum (smooth curve) is derived by curve-fit of experimental spectra and is given by $S_1=h^2 \Omega_o^2/(\Omega_o^2+\Omega^2)^{3/2}$ where Ω is the angular spatial frequency or wavenumber. The correlation function, derived by cosine transform of S_1, is $\Psi(r)=h^2(\Omega_o r)\,\mathbf{K}_1(\Omega_o r)$, where $\mathbf{K}_1$ is the modified Bessel function, $L=2/\Omega_o$ is the correlation length and h is the standard deviation about mean draft. Azimuthal distribution is taken to be isotropic and the 2-dimensional spectrum, derived by the J_o Bessel transform, becomes $S_2=2\,h^2 \Omega_o^2/(\Omega_o^2+\Omega^2)^2$ where $\int_o^\infty \Omega\, d\Omega\, S_2(\Omega)=h^2$.

Ice profiles of draft were analyzed in approximately 1 km segments and averaged over 10 contiguous segments. The power spectra and correlation functions were calculated numerically. Correlation lengths were measured by fitting correlation curves with the analytic model.

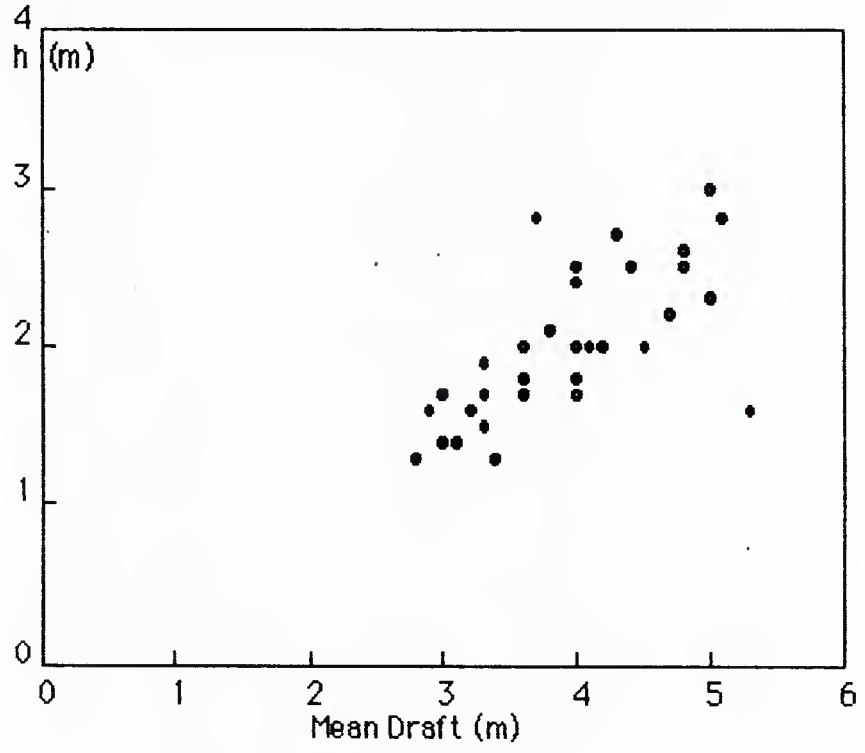

Figure 4: Standard deviation vs mean draft

The standard deviation vs mean draft data in Figure 4 show quite high correlation. The RMS value for the set is h=2m. Figure 5 shows negligible correlation between L and mean draft. The average of the set is L= 44m. Figure 6 shows no significant correlation between L and h also.

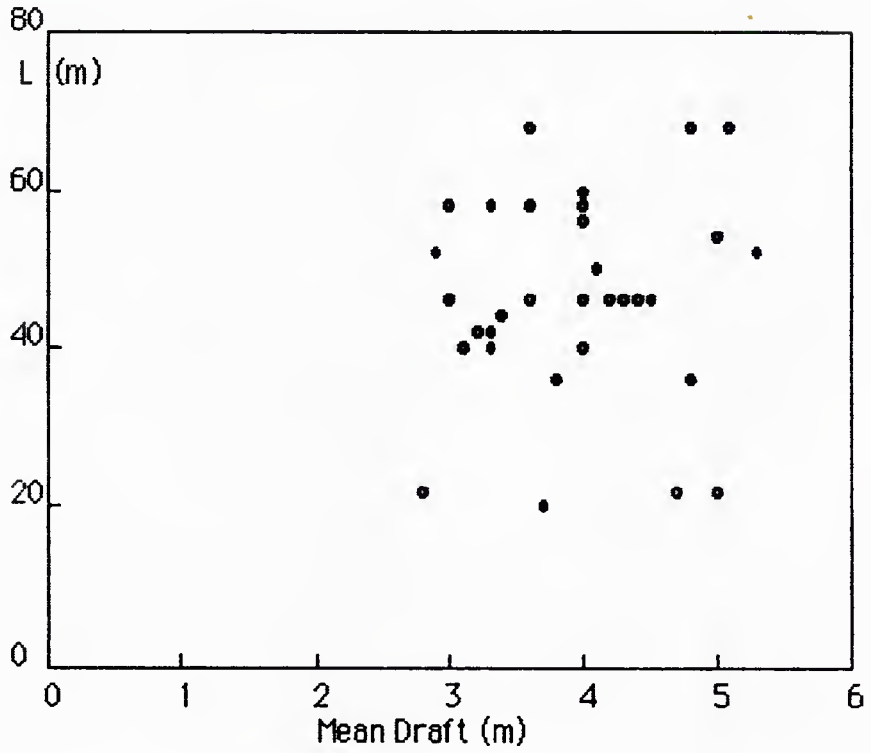

Figure 5: Correlation length vs mean draft

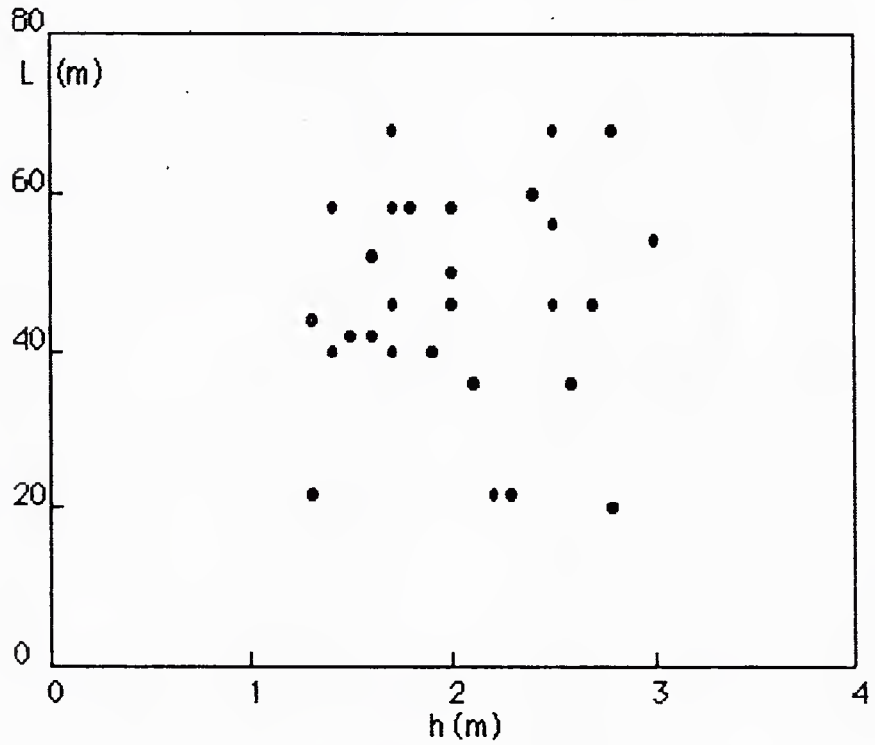

Figure 6: Correlation length vs standard deviation

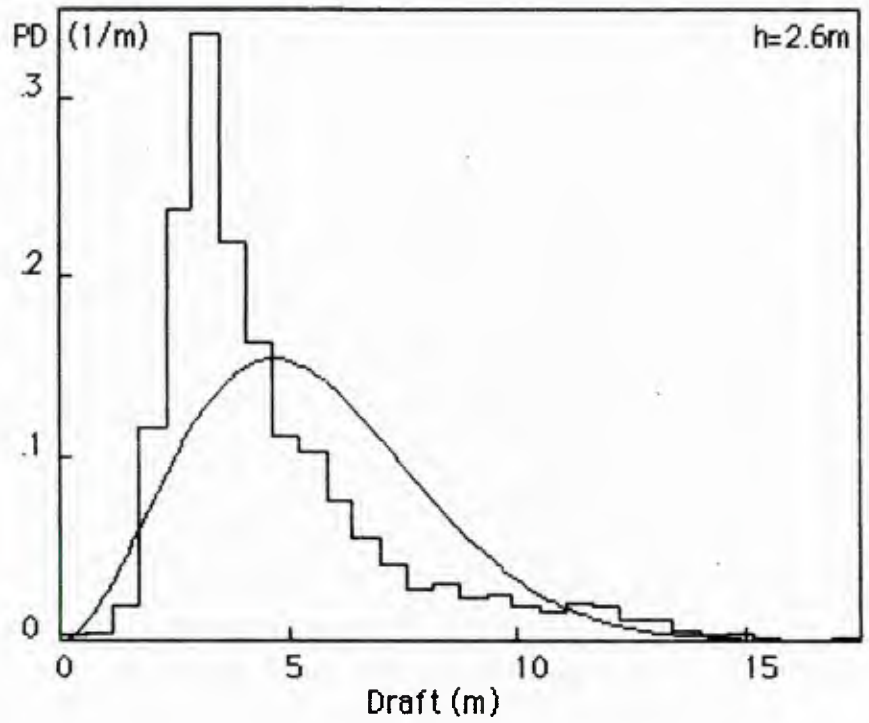

Figure 7: PDF of draft-model and data

Analysis of a "shot-noise" model of the underice roughness by Nuttall [6] indicates that the probability density function (PDF) of draft should be similar to a Rayleigh distribution.

In Figure 7, the expected PDF (smooth curve) is compared with typical data. Both have been normalized to unit area and have the same standard deviation. Note that the mean draft of the model is clearly greater than that of ice and the PDF is less highly peaked. The purpose of the composite model is to reconcile these discrepencies.

The high degree of correlation between standard deviation and mean draft in Figure 4 indicates that the underice roughness is not statistically homogeneous. There appear to be significant variations in the roughness parameters that occur on a scale much larger than the correlation length and this suggests that modeling roughness as a single-population may not be appropriate.

The ice pack shows large areas of comparative smoothness interspersed by areas of high roughness. We will consider a composite model composed of two populations having different degrees of roughness and occupying different contiguous areas. Note that this differs from the conventional sea-surface composite model in which two are superposed.

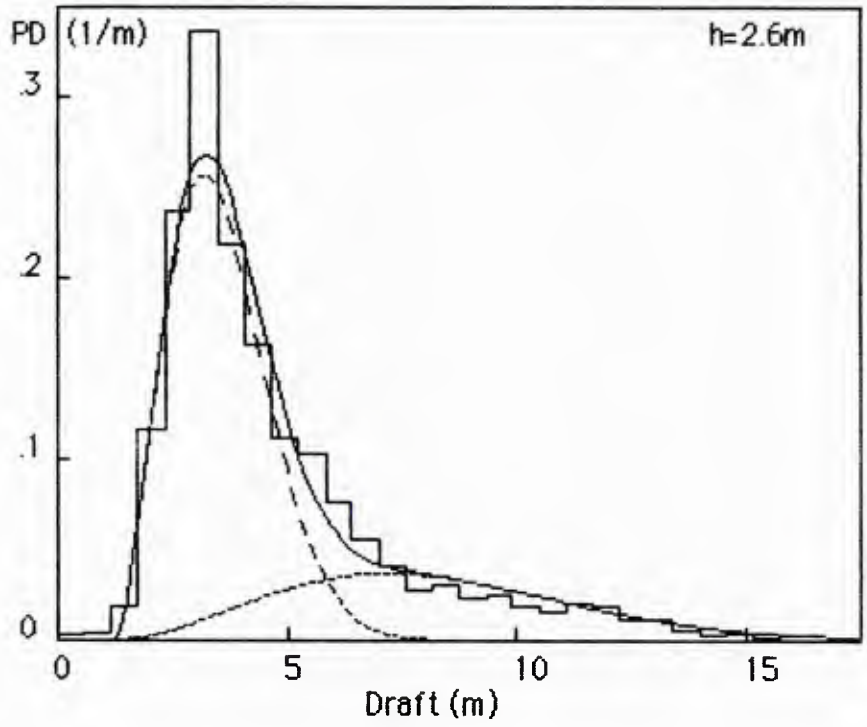

Figure 8: PDF of draft-composite model and ice data

In Figure 8, the data are fitted using two distributions having different standard deviations; i.e. 1.1m and 3.3m, shown by the dashed curves. The weighting factors are 0.7 and 0.3, respectively. A bias of 1.5m has been added to improve the fit and the respective mean drafts are approximately 4m and 8m. The sum of the two components, shown by the solid curve, is now in fairly good agreement with the data.

Scattering loss is proportional to the variance h^2. When the correlation lengths of the two components are equal, the area-weighted variances are additive. The variance of mean draft has a much greater correlation length, which will reduce its contribution in Marsh theory. This component will appear as an increase in spectrum level at very low wavenumbers and a slow decay in the correlation function at long lags. Both effects have been noted in the experimental data.

While the composite model appears somewhat more realistic than the homogeneous model, the effects on scattering appear to be negligible, at least in the free-surface case. Concentration of roughness in one area at the expense of another does not increase low-frequency loss significantly in this approximation. It will be seen later, however, that the effects do become important when impedance is taken into account.

Scattering-loss theory

The Marsh formula for the coherent energy reflection coefficient can be written as Q=1-SL, where SL≈3.3 sinθ $(kh)^2/(kL)^{1/2}$, θ is grazing angle and k is acoustic wavenumber. To allow some extension beyond the limits of perturbation theory, the loss is approximated as 4.34 SL (dB/bounce).

The skip-distance in a surface-channel is given by 2c tanθ/g where c is the sound-speed and g is the gradient. Loss vs range is then approximately independent of ray-angle for small angles. For g=.06/sec, h=2m and L=44m, the attenuation becomes A≈1.5 $f^{3/2}$ dB/km where f is the frequency in kHz. This result is in good agreement with the data-trend of Figure 2 but is too low by roughly a factor of two. More exact analysis, using computer codes for calculating propagation loss and adding the reflection loss per bounce, show that the approximation is quite accurate.

The fact that the Marsh formula involves the correlation length implies that the scatter beam-pattern is important in this approximation régime. For kL<2π the beamwidth of the scattered energy tends to become large. Much of the energy will then escape from the channel at each incidence and be absorbed by the bottom.

For kL>2π, the scattered energy approaches specular and loss goes as k^2, which is characteristic of the Eckart [7] régime. While perturbation theory requires kh sinθ <<1, the Eckart solution is not limited by this criterion and the loss approximation becomes "exact".

In the low frequency limit where kL<<2π, scattering becomes diffuse and the loss goes as k^4. This is characteristic of Rayleigh scattering where all scales become small compared to acoustic wavelength. For the correlation length 44m, rolloff becomes important below about 50 Hz.

A formula based on the method of small perturbation (MSP) and valid in all domains will be used. Equation 9.6.3 of Brekhovskikh and Lysanov [8] calculates scattering loss by a 2-dimensional integral over the surface spectrum. In Appendix A, we derive an equivalent integral over scattering angles, which shows where the energy goes. Using the analytic spectrum and assuming isotropicity reduces the computational problem to a single integral over depression angle. Numerical evaluation of the B&L integral has been found to give identical results.

The coherent reflection coefficient Q is defined here as the fractional intensity of the reflected wave in the specular direction. It is assumed, temporarily, that the interface acts like a rough free-surface. Assuming small displacements compared to the vertical component of the acoustic wavelength, MSP theory yields the following result:

$$SL = k^4 \sin\theta \int_0^{\pi/2} d\theta' \sin^2\theta' \cos\theta' \int_{-\pi}^{\pi} d\phi \int_0^{\infty} r\,dr\,\Psi(r) J_0(\Omega r)/2\pi$$

$$\Omega = k\left[\cos^2\theta + \cos^2\theta' - 2\cos\phi\cos\theta\cos\theta'\right]^{1/2}$$

$$k = 2\pi f/C \qquad \Psi(r) = h^2\,\Omega_0\, r\, K_1(\Omega_0 r)$$

$$\int_0^{\infty} r\,dr\,\Psi(r) J_0(\Omega r) = 2h^2\Omega_0^2/(\Omega_0^2+\Omega^2)^2 \equiv S_2$$

First Integral

$$2\int_{-\pi}^{\pi} d\phi\, S_2/\pi = 4h^2(1+u^2)/\Omega_0^2\left((1+u)^2 - v^2\right)^{3/2} \equiv S_1'$$

$$u = (k/\Omega_0)^2(\cos^2\theta + \cos^2\theta') \qquad v = 2(k/\Omega_0)^2\cos\theta\cos\theta'$$

Second Integral

$$SL = k^4 \sin\theta \int_0^{\pi/2} d\theta' \sin^2\theta' \cos\theta'\, S_1'$$

Final numerical integral

Eckart	$SL = (2kh\sin\theta)^2$	$Ru \gg 1$	$kL \gg 1$
Marsh	$SL = 3.3(kh)^2\sin\theta/(kL)^{1/2}$	$Ru \ll 1$	$kL \gg 1$
Rayleigh	$SL = (2/3)(kh)^2(kL)^2\sin\theta$		$kL \ll 1$

$$L = 2/\Omega_0 \qquad Ru = kL\sin^2(\theta/2)$$

Asymptotic Approximations

The theory is based on Bragg-scatter matching between acoustic (k) and surface (Ω) wavenumbers as a function of the incident grazing-angle θ, the scatter grazing-angle θ' and the azimuthal angle ϕ relative to the direction of the incident plane-wave.

The first (radial) integral yields the 2-dimensional analytic spectrum. The second (azimuthal) integral yields a function similar to the analytic 1-dimensional spectrum. This leaves only a single integral over scatter angle θ' to evaluate numerically. Asymptotic solutions provide a check on results. The parameter Ru is a measure of forward-scattering directivity and occurs in Rutherford scattering.

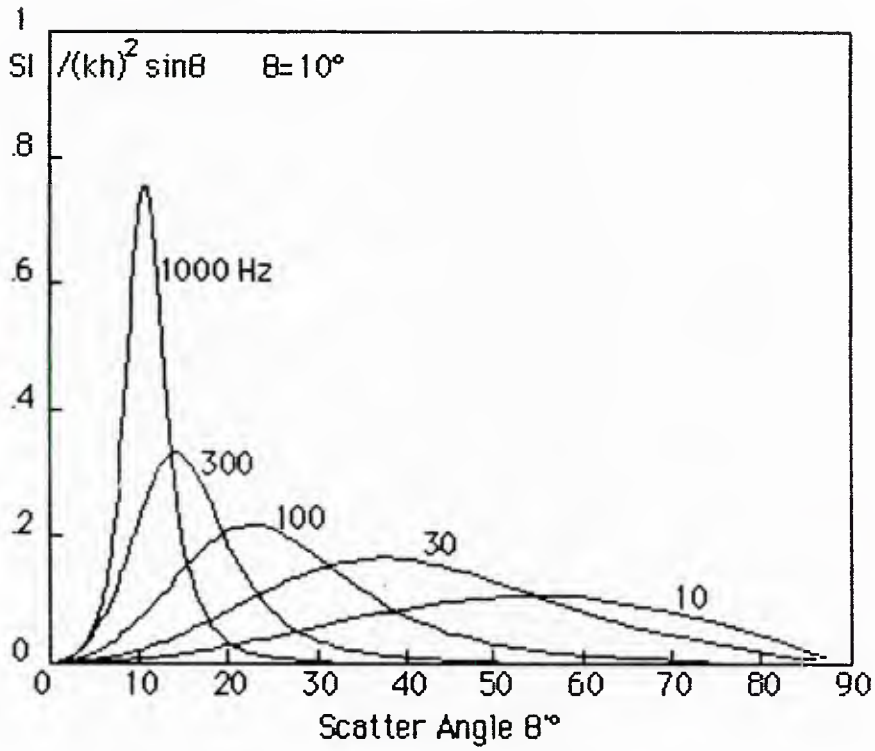

Figure 9: Ice spectrum integrands vs scatter angle.

The curves of Figure 9 show the scatter-loss integrands vs the scatter grazing-angle in the frequency range 10-1000 Hz for an incident grazing angle 10°. Results have been normalized by dividing by $(kh)^2 \sin\theta$ in order to limit the scale. Scattering is seen to become diffuse at low frequencies and to approach specular at high frequencies.

The integrands can be considered as scatter from an area of radius equal to the correlation length and "coherent" with the incident plane-wave. The summation over a random ensemble of areas makes the average scattered energy incoherent.

The integrands resemble beam patterns; however, they are not the usual cross-sections but are azimuthally-integrated values and multiplication by $\cos\theta'$ is required for flux integration. At low frequency, the integrand approaches the vertical-dipole pattern $\sin^2\theta'$ multiplied by $\cos\theta'$.

From the integrands, one can estimate the fraction of scattered energy remaining in the channel. For a critical trapping angle of 10°, for example, more than 1/2 would be lost at each reflection at frequencies below 1 kHz. After multiple reflections, incoherent levels should then converge rapidly to negligible values, providing that the bottom is sufficiently lossy.

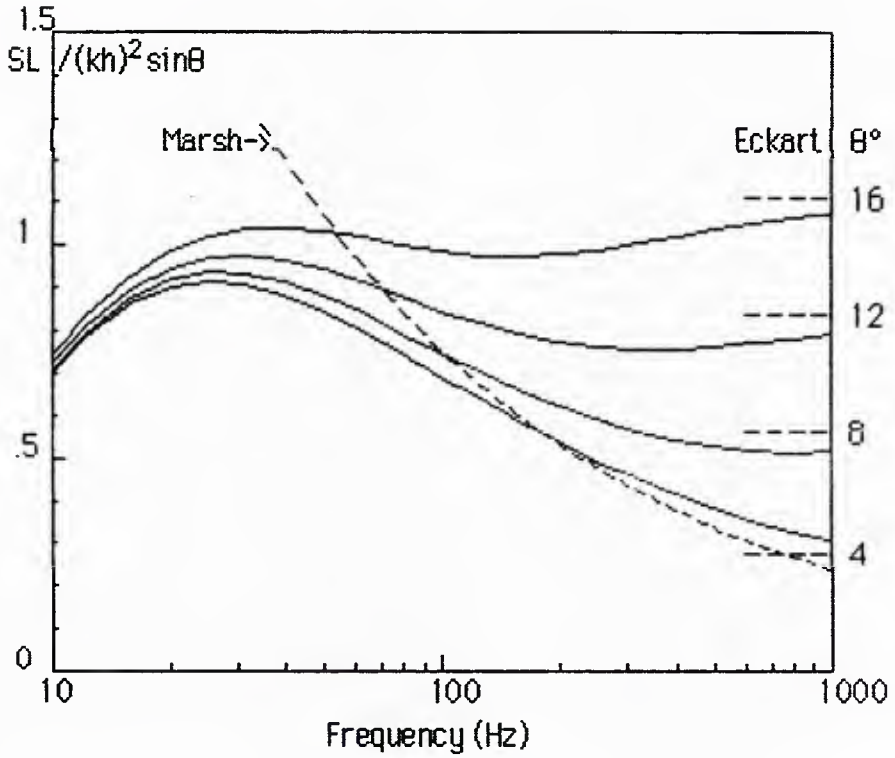

Figure 10: Ice spectrum scattering coefficients vs frequency.

In Figure 10, the values obtained by numerical integration are plotted vs frequency for selected grazing angles between 4 and16°, which represents the domain of interest for long-range propagation. Values have again been normalized by dividing by $(kh)^2\sin\theta$, making both the Marsh and Rayleigh asymptotes independent of grazing angle. The dashed lines at the right are the Eckart asymptotes.

Note that the Marsh curve tends to become inaccurate below 100 Hz in the Rayleigh régime and also at high frequency in the Eckart régime.

Loss estimates below 100 Hz have already proven too low by more than a factor of two in the Marsh approximation. The integral values become even smaller with decreasing frequency. Since the conditions for MSP theory are evidently not exceeded in this range, there is little reason to suspect errors in the approximations.

Failure to account for attenuation indicates that impedance effects must be involved. Dissipation within the ice layer is a potential loss mechanism. However, much higher backscatter levels are also observed experimentally than predicted by free-surface theory, which suggests that the effects of impedance on scattering must be more significant.

Impedance

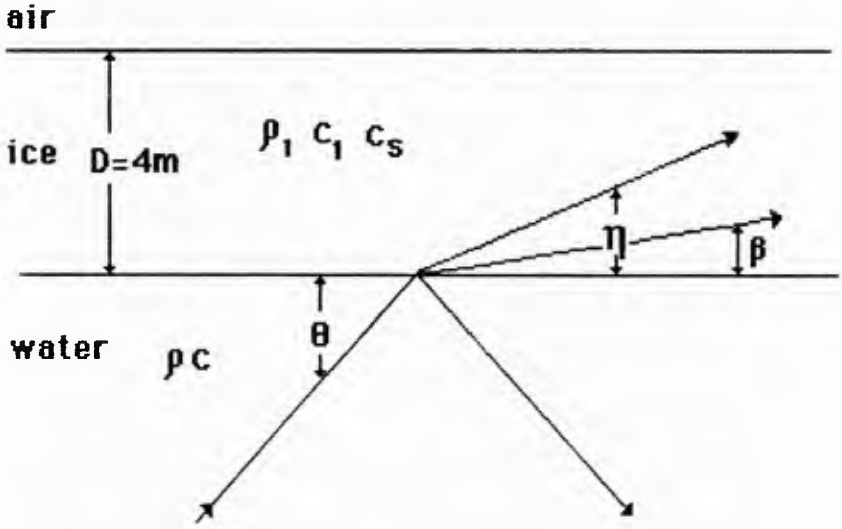

ρ=density C=compressional speed C_S=shear speed

$$M = \frac{c_1 \cos^2(2\eta)}{\sin\beta \tan(k_1 D \sin\beta)} + \frac{c_s \sin^2(2\eta)}{\sin\eta \tan(k_s D \sin\eta)}$$

$$N = \frac{c_1 \cos^2(2\eta)}{\sin\beta \sin(k_1 D \sin\beta)} + \frac{c_s \sin^2(2\eta)}{\sin\eta \sin(k_s D \sin\eta)}$$

$$Z_r + iZ_i = i\rho_1 (N^2 - M^2)/M \qquad Z_0 = \rho\omega D$$

Figure 11: Interface impedance model.

The impedance problem is illustrated in Figure 11 where η and β are the shear and compressional grazing-angles in ice, respectively. Neglecting air impedance and dissipation, reflection is total. Dissipation is included by taking c_s and c_1 to be complex, as described in Appendix B.

The plane-wave reflection coefficient then becomes [2]:

$$Rz = [-1 + \sin\theta\,(Zr+iZi)/\rho c]/[1 + \sin\theta\,(Zr+iZi)/\rho c]$$

In order to get any scattering by interfacial roughness, there must be an impedance discontinuity at the boundary. It is instructive to normalize relative to Zo. Consider the lossless case. When $Zi/Zo \to 0$, there is perfect reflection with a phase reversal and the interface becomes effectively pressure-release. For $Zi/Zo \to \rho_1/\rho$, the interface discontinuity is inertial and vanishes for equal densities in the two media.

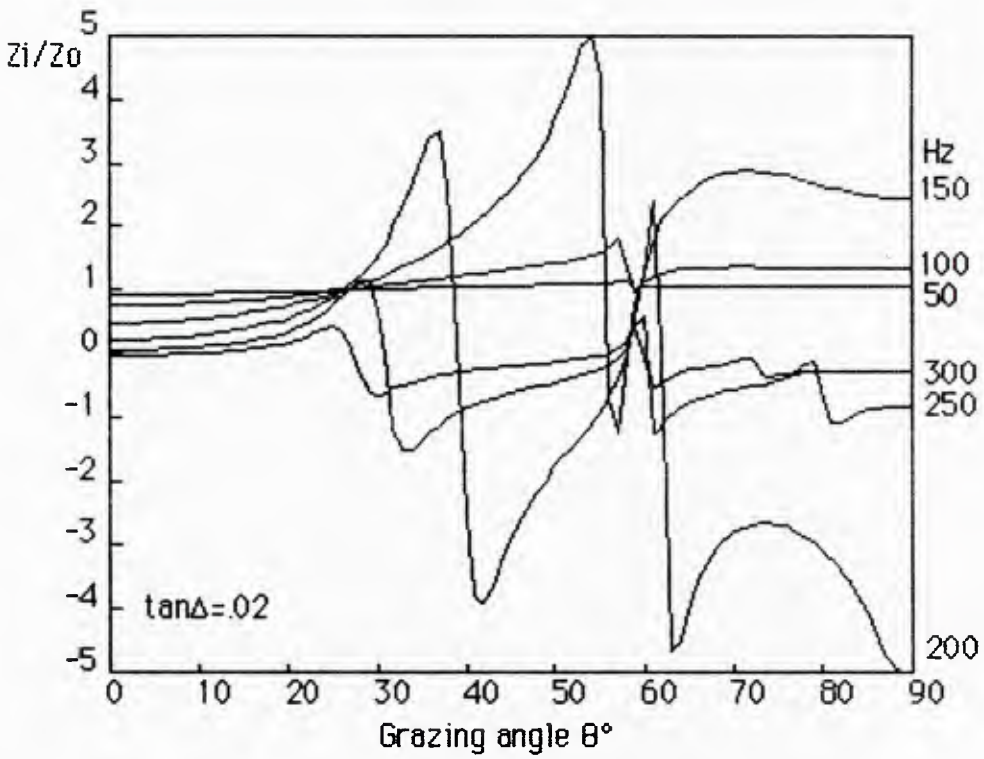

Figure 12 Impedance ratio Zi/Zo vs grazing angle.

Figure 12 shows Zi/Zo as a function of grazing angle for the frequency range 50 to 300 Hz in 50 Hz steps. Compressional and shear speeds in ice have been taken as 3000 and 1800 m/s, respectively, with the shear loss tanΔ=.02. For simplicity, the same value is used for compressional loss, but effects are minor.

At low frequencies, $Zi/Zo \rightarrow \rho_1/\rho$ for all angles. As frequency increases, resonance effects of the compressional and shear waves become evident around the critical angles 60° and 33°, respectively. For grazing angles greater than 60°, compressional effects dominate and reactance oscillates between inertial (+) and stiffness (-) control. Similar effects are seen between 30° and 60° where shear effects dominate. Below 30°, inertial effects dominate, diminishing to zero as the shear resonance begins to develop.

In the Arctic sound-channel propagation problem, grazing angles less than 15° and frequencies below 1 kHz are of interest at longer ranges. In this domain, there is a simple transition from the mass-loaded condition, with negligible boundary discontinuity, to an effectively pressure-release condition with perfect reflection at the interface. The problem is that the transition occurs at such high frequencies.

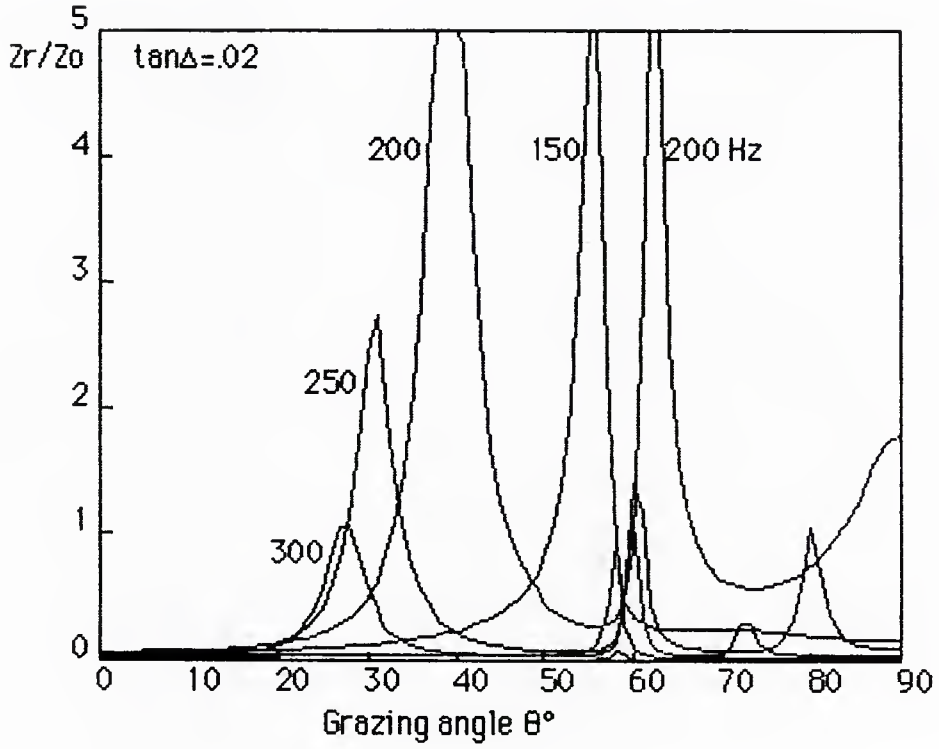

Figure 13: Impedance ratio Zr/Zo vs grazing angle.

Figure 13 shows curves of the impedance ratio Zr/Zo for tanΔ=.02. It is clear that internal losses are small except at resonances, where multiple internal reflections occur. Mass loading become dominant at small grazing angles and the elastic properties vanish. In this régime, dissipation losses become quite small.

The ratio Zi/Zo is most important in the case of vertical-dipole scatter because it is a measure of the phase shift of the reflected wave relative to the ice/water interface. No phase shift means perfect reflection at the interface while a delay equal to that in a water layer of equal thickness means that the ice/water impedance discontinuity vanishes. Corresponding effects in the time domain are shown in Appendix C.

Perturbation analysis for finite impedance [9] is outlined in Appendix D. Results show that the vertical-dipole component of scatter loss is simply the free-surface integral with the integrand multiplied by the effective reflection coefficient R_o^2.

The analysis also shows that there is second vertical-dipole component of the velocity type, analogous to a piston in a baffle. The scatter loss for the infinite-impedance case involves a similar integral. For the finite-impedance boundary, the integrand is simply multiplied by the effective reflection coefficient R_∞^2.

Vertical-dipole models

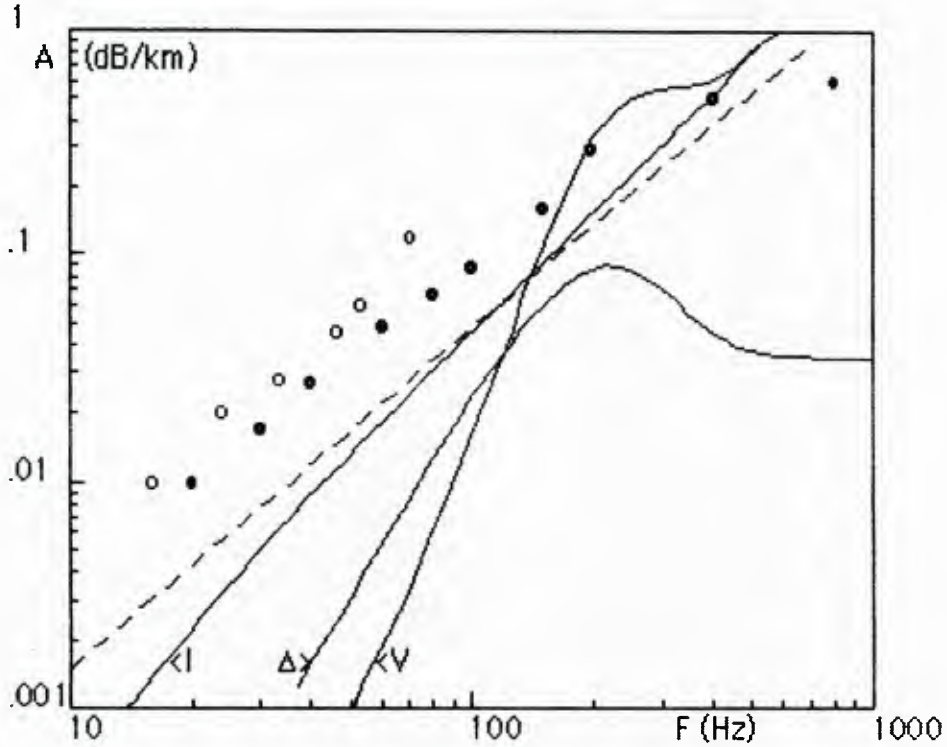

Figure 14: Attenuation-vertical dipole models.

Figure 14 compares predictions of the various vertical-dipole models to the attenuation data. The gradient is taken as 0.06/s and the grazing angle as 8°, making the skip-distance roughly 7 km.

The dashed line is the Marsh formula. Note that the predictions are low by more than a factor of two at low frequencies.

Curve I is the numerical-integration result for the free-surface model. The slow low-frequency rolloff involves transition to the Rayleigh régime where scattering becomes diffuse. A slow transition to the Eckart régime of "specular" scatter is seen at the higher frequencies.

Curve V shows the effects of the impedance factor Ro^2 on curve I. Note that the attenuation decreases rapidly in the mass-loading régime below about 200 Hz. The "piston" component turns out to be negligible throughout the entire range and is omitted.

Dissipation loss is calculated from the magnitude $|Rz|^2$. Curve Δ shows the results for $\tan\Delta=.02$. Total attenuation is then the sum of Δ and V.

Clearly, the results do not agree with the data and "improvements" seem to have made matters much worse. Analysis of seismometer data from experiments by Buck [10] suggests a possible reason for the failure.

Seismometer experiments

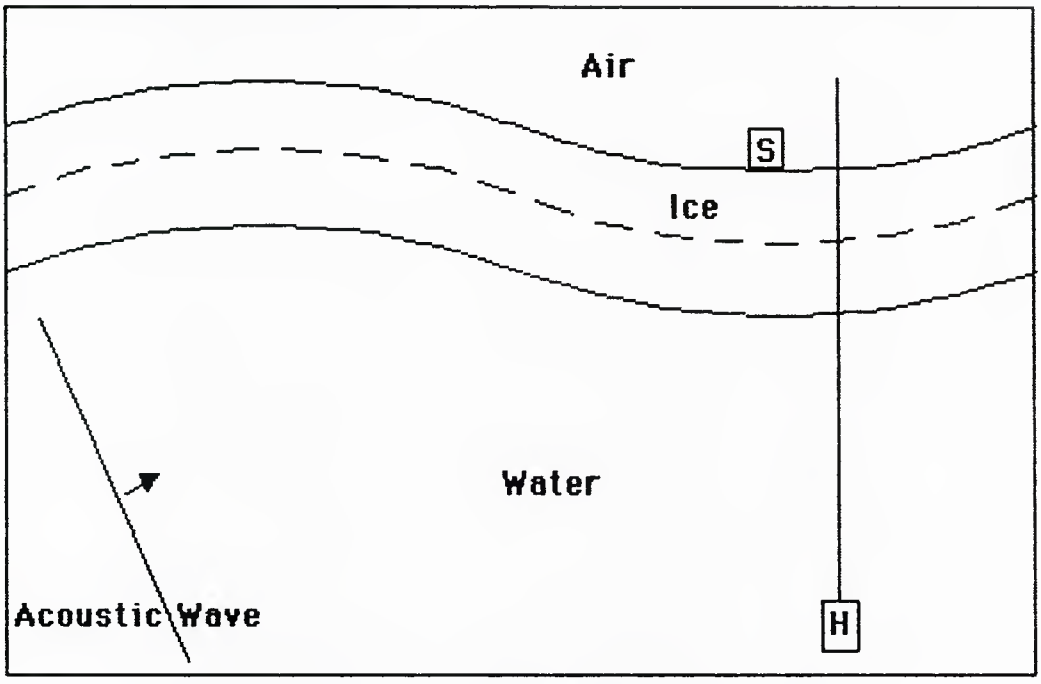

Figure 15: Seismometer/hydrophone experiment.

Perfect acoustic contact at the ice/water interface has been assumed. Trapped air could make the impedance very low. Comparison of hydrophone and seismometer signals shows that this is not the case.

Figure 15 shows the response (greatly exaggerated) of the ice layer to an incident plane-wave. The transfer function of pressure to surface velocity can be estimated by comparing the signals received from a distant source. At low frequencies and grazing angles, thin-plate theory is valid and the motion of the median plane (dashed line) is vertical. Neglecting the small difference in densities, the vertical component of surface velocity is the same as the free-surface case: $U_v \approx (2P/\rho c)\sin\theta$, where P is the pressure. The horizontal component is $U_h \approx iU_v(kD/2)\cos\theta$, where D is the thickness.

Figure 16 compares hydrophone and vertical seismometer signal levels at 25 and 50 Hz. The equivalent plane-wave pressure is estimated from the hydrophone response at the experimental depth 100m. Agreement with the estimated response for $\theta=8°$ (dashed line) is seen to be reasonable.

Figure 17 compares the horizontal and vertical-seismometer signals. Estimates for the experimental condition D=5m are shown by the dashed lines. The fact that horizontal velocities are much greater than predicted indicates a "rocking" motion involving slopes. The associated horizontal-dipole term of Appendix D must therefore be considered.

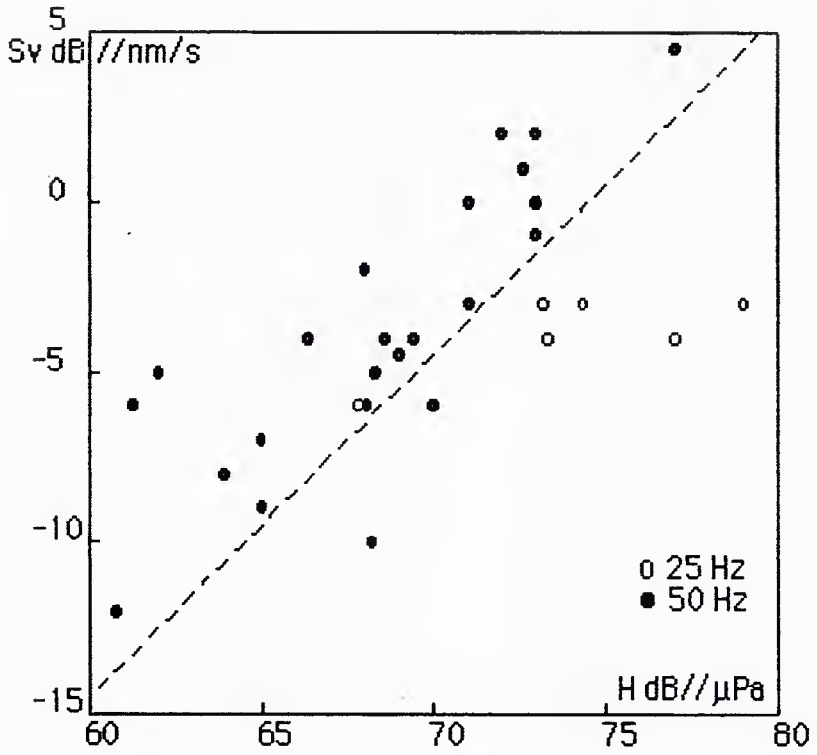

Figure 16: Vertical seismometer vs hydrophone data.

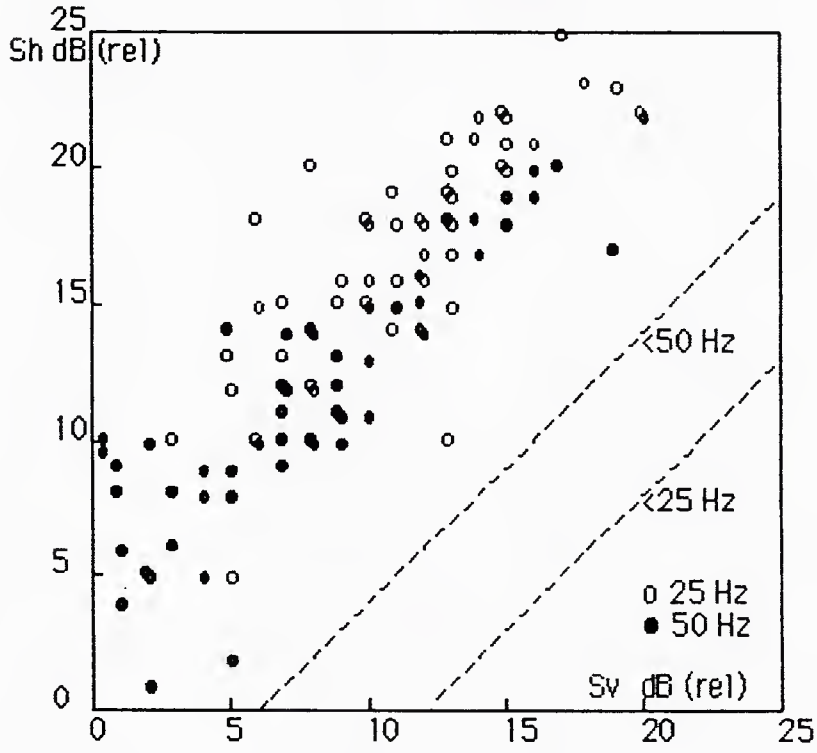

Figure 17: Horizontal vs vertical seismometer data.

General Impedance models

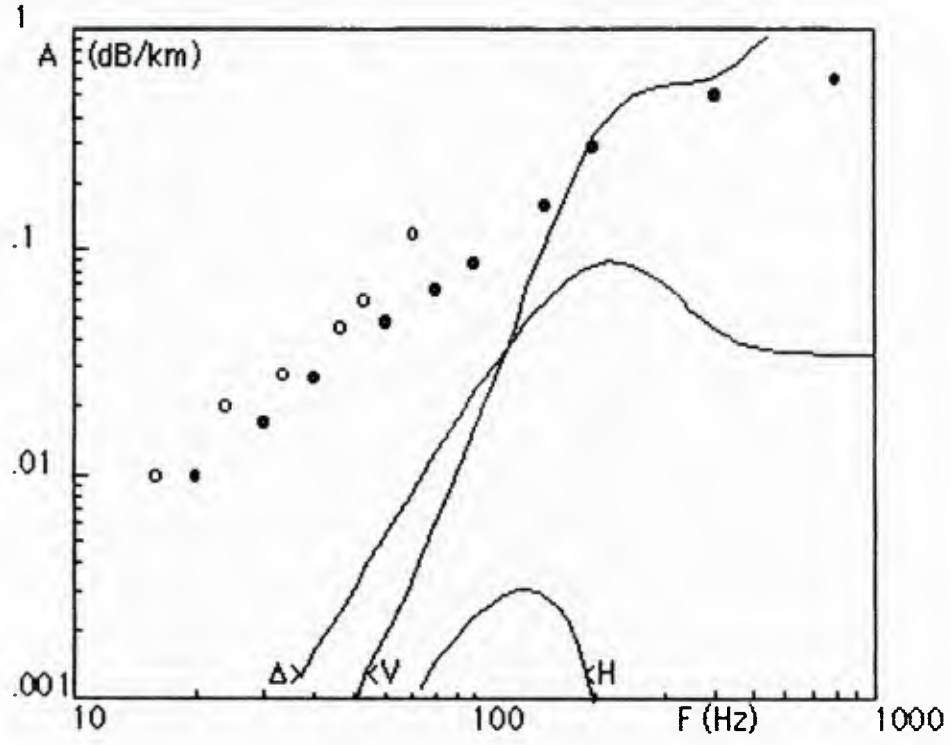

Figure 18: Attenuation-general impedance model.

The scatter-loss integral for the horizontal-dipole case in Appendix D is:

$$SL \approx 2\, k^2 \cos\theta \cot\theta \int_0^{\pi/2} d\theta' \cos\theta' R_\infty^2 \int_{-\pi}^{\pi} d\phi\, \Omega_x^2\, S_2(\Omega)/\pi$$

where R_∞^2 is the effective reflection coefficient for the rigid-boundary solution and $\Omega_x = k(\cos\theta - \cos\theta'\cos\phi)$ is the Bragg-scattering condition associated with the x component of the slopes. Since an analytic solution of the ϕ integral has not been found, the double integral must be calculated numerically. Note that $SL \to \infty$ as $\theta \to 0$ only for the rigid-boundary case and remains finite for finite impedance since R_∞ contains a $\sin^2\theta$ term.

The attenuation curves shown in Figure 18 are calculated for the same conditions as Figure 14. Curve H is the horizontal-dipole component, curve V is the vertical-dipole component and curve Δ is dissipation.

It is clear that the horizontal-dipole scatter component is a significant attenuation mechanism at the lower frequencies. However, predictions do not agree with the data in this range. Sensitivity to ray angle should be noted. Since angle effects are quite complicated, a detailed analysis by either normal-mode or numerical methods may be indicated. Sensitivity to the PDF of draft is more readily examined.

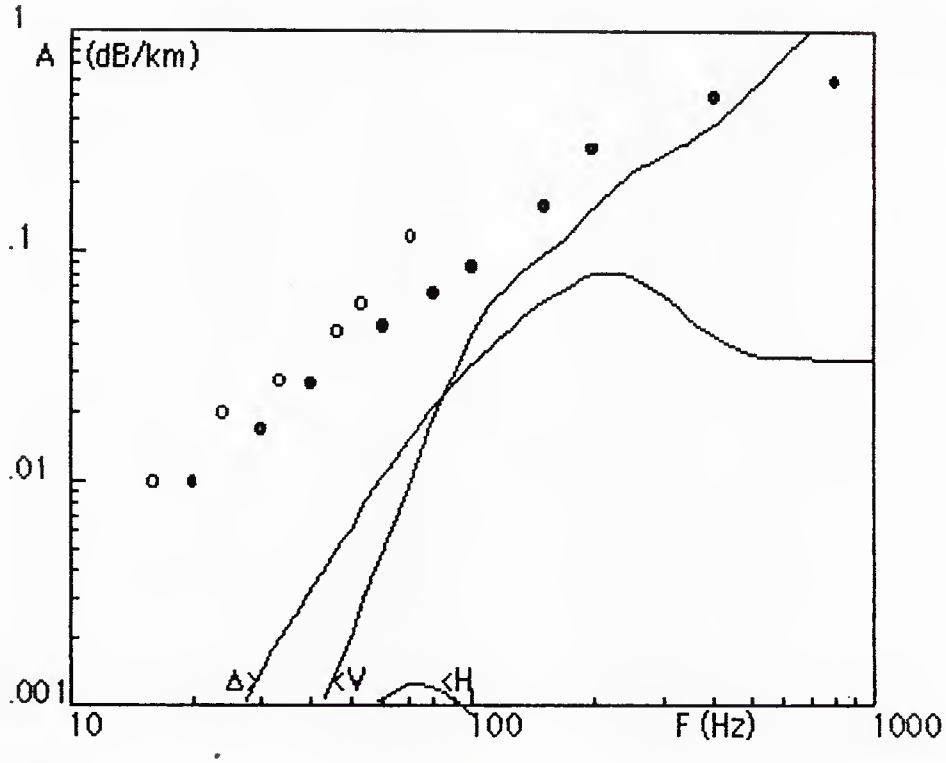

Figure 19: Composite general-impedance model.

Figure 19 shows that predictions can be put into only slightly better agreement with data using the composite PDF model of Figure 8; i.e. a bimodal model with standard deviations 1.1m and 3.3m, weighting factors 0.7 and 0.3 and mean drafts 4m and 8m, respectively. Values for the two modes were calculated numerically and the area-weighted losses added.

The main effect of the composite model is due to the impedance of the dominant 8m component of draft. The higher impedance causes an increase in low-frequency loss and a reduction at high frequencies, resulting in a slightly better fit to the data.

Obviously, the agreement can be improved by further modification of the PDF model; e.g. a multimodal model can be devised that might provide a better overall fit. However, in view of the problems involving ray-angle sensitivity, as well as questions about data accuracy, such refinements do not appear justified at this time nor are the prospects for success very encouraging.

Conclusion

It is apparent from this analysis that, although scattering at the rough ice/water interface remains the most likely mechanism for the excess attenuation noted in Arctic propagation experiments, consideration of finite-impedance effects does not appear to account for the data.

The ice-reflectivity problem has turned out to be quite complex. At finite-impedance boundaries, scattering involves horizontal-dipole and "piston" components in addition to the usual vertical-dipole component associated with free surfaces. While the horizontal-dipole may be the most significant loss mechanism at lower frequencies, predicted values are still much too low.

The scattering theory is based on the usual Bragg condition wherein the scatter angles are determined by matching of the acoustic and roughness wavenumbers. Rigorously, the MSP approximation requires small values of the Rayleigh-roughness parameter. This is violated mainly in the Eckart régime, where the solution is not limited by the criterion. Approximation errors are not expected to be serious much below 1 kHz.

Effects of finite impedance on vertical-dipole scattering are quite clear at lower frequencies and grazing angles where inertial forces dominate. In this régime, scattering arises from spatial variations in mass. Since ice displaces an equal (almost) mass of water, scattering tends to vanish. The scatter loss (dB/bounce) is approximately proportional to grazing angle. The skip distance has similar dependence, making loss in dB/km nearly independent of angle.

In the horizontal-dipole case, the dB/bounce loss is a more complex function of grazing angle, making the analysis of propagation much more sensitive to angle effects. However, since predictions are far too small in the inertial régime below about 100 Hz for all reasonable angles, current prospects for an adequate predictive model appear rather remote.

References

1. H. W. Marsh, M. Schulkin and S. G. Kneale, "Scattering of Underwater Sound by the Sea surface", J. Acoust. Soc. Am. 33, 334-340 (1961).

2. L. Brekhovskikh, Waves In Layered Media, (Academic Press, New York 1982) second edition, Ch.10, pp 70-71.

3. W. A. Kuperman and H. Schmidt, "Rough Surface Elastic Wave Scattering in a Horizontally Stratified Ocean", J. Acoust. Soc. Am. 79 1767-1777 (1986)

4. Underwater Sound in the Arctic, NUSC Scientific & Technical Report, (1984) contains reprints of the following pertinent references:
   H. W. Marsh and R. H. Mellen, "Underwater Sound Propagation in the Arctic Ocean", J. Acoust. Soc. Am. 35 552-563 (1963)
   R. H. Mellen and H. W. Marsh, "Underwater Sound Reverberation in the Arctic Ocean", J. Acoust. Soc. Am. 35 1645-1648 (1963)
   R. H. Mellen and H. W. Marsh, "Underwater Sound in the Arctic Ocean" AVCO/MEO report to USNUSL, August 1965
   R. H. Mellen, "Underwater Sound in the Arctic Ocean" USN/JUA 16 247-259 (1966) (unclassified)

5. F. R. DiNapoli and R. H. Mellen, "Low-Frequency Attenuation in the Arctic Ocean", in Ocean Seismo-Acoustics, eds. T. Akal and J. M. Berkson (Plenum Press, New York, 1986)

6. A. H. Nuttall, "Under-Ice Roughness: Shot Noise Model" NUSC Technical Memorandum TM-841208, 31 Dec. 1984.

7. C. Eckart, "The Scattering of Sound from the Sea Surface", J. Acoust. Soc. Am. 25 566-570 (1953)

8. L. Brekhovskikh and Y. Lysanov, Fundamentals of Ocean Acoustics, (Springer-Verlag, New York 1982), Ch. 9.

9. F. I. Kryazhev and V. M. Kudryashov, "Sound Field in a Waveguide with a Statistically Rough Admittance", Sov. Phys. Acoust. 30 391-393 (1984)

10. B. M. Buck, Polar Research Laboratory (personal communication).

Appendix A: Free-surface theory

Perturbation theory for scattering at a free surface is treated in Ref. 8. The surface boundary condition is given by Eq. 9.2.4 as:

$$p + \zeta \, \partial p/\partial z = 0 \qquad 1A$$

where p is the acoustic pressure, ζ is the surface displacement and z is depth. Let $p = p_0 + p_s$ where p_0 is the pressure for $\zeta = 0$ and p_s is the scattered pressure for $\zeta \neq 0$. Equating the zero and first-order perturbation terms as in Eqs. 9.2.6-7, we have:

$$p_0 = 0 \qquad p_s + \zeta \, \partial p_0/\partial z = 0 \qquad 2A$$

The scattered field corresponds to vertical-dipole reradiation. Instead of following the derivation of Ref. 8, we take the more physically oriented approach outlined below.

The farfield component of the Green's function for a scattering element and surface image yields the differential scattered pressure:

$$dP_s \approx ikP_0 \sin\theta \, dA \, [\exp(ik\zeta \sin\theta') - \exp(-ik\zeta \sin\theta')] \exp(ikR)/2\pi R \qquad 3A$$

where k is the acoustic wavenumber, P_0 is the incident pressure, θ and θ' are the incident and scatter grazing-angles, dA is an element of surface area and R is the radius to a distant field point. For small values of the exponential arguments, Eq. 3A becomes:

$$dP_s \approx -P_0 k^2 \zeta \sin\theta \sin\theta' \, dA \exp(ikR)/\pi R \qquad 4A$$

For a plane wave incident in the x direction, we then have:

$$P_s \approx -P_0 k^2 \int dx \int dy \, \zeta(x,y) \sin\theta \sin\theta' \exp[ik(R + x\cos\theta)]/\pi R \qquad 5A$$

where x,y are the surface coordinates. The scattered field is seen to be equivalent to broadside (y integral) and vertically-steered (x integral) reradiation by a phased-array of vertical dipoles.

The Bragg-scatter condition for matching the wavenumber spectrum of $\zeta(x,y)$ is $\Omega_x = k(\cos\theta - \cos\theta' \cos\phi)$ and $\Omega_y = k \cos\theta' \sin\phi$. Continuous spectra involve mean-squared values and spatial convolution of Eq. 5A is required. For the case of isotropic roughness, it can be shown that the result is:

$$P_s^2(\theta',\phi) \approx P_0^2 A_0 k^4 \sin^2\theta \sin^2\theta' \int_0^\infty r\,dr \, \Psi(r) J_0(\Omega r) / (\pi R)^2 \qquad 6A$$

where $\Omega = (\Omega_x^2 + \Omega_y^2)^{1/2}$, $r = (x^2+y^2)^{1/2}$, $\Psi(r)$ is the correlation function of ζ, $\sin^2\theta'$ is the scattering beam-pattern of an element dA, A_0 is the effective "coherent" area and $\Omega = k\,[\cos^2\theta + \cos^2\theta' - 2\cos\theta' \cos\theta \cos\phi]^{1/2}$ is the Bragg wavenumber condition.

The total flux scattered by the area is:

$$P_s^2 A_0 \approx 2\pi R^2 \int_0^{\pi/2} d\theta' \cos\theta' \int_{-\pi}^{\pi} d\phi\, P_s^2(\theta',\phi) \qquad 7A$$

We defined the intensity reflection-coefficient as Q=1-SL, where SL is scattering loss. Conservation of total vertical flux at the surface requires $P_0^2(1-Q)\sin\theta = P_s^2$. Averaging over a random ensemble of areas and taking $SL=\langle P_s^2\rangle / P_0^2 \sin\theta$ gives:

$$SL \approx 2k^4 \sin\theta \int_0^{\pi/2} d\theta' \sin^2\theta' \cos\theta' \int_{-\pi}^{\pi} d\phi \int_0^{\infty} r\,dr\, \Psi(r)\, J_0(\Omega r)/\pi \qquad 8A$$

The radial integral gives the surface spectrum $S_2(\Omega)$ and Eq. 8A becomes:

$$SL \approx 2k^4 \sin\theta \int_0^{\pi/2} d\theta' \sin^2\theta' \cos\theta' \int_{-\pi}^{\pi} d\phi\, S_2(\Omega)/\pi \qquad 9A$$

Equation 9A is equivalent to Eq. 9.6.3 of Ref. 8. In terms of the present model parameters, the B&L integral is:

$$SL \approx 2k^2 \sin\theta \int \Omega\, d\Omega \int d\phi\, [\sin^2\theta + 2(\Omega/k)\cos\theta\cos\phi - (\Omega/k)^2]^{1/2}\, S_2(\Omega)/\pi \qquad 10A$$

where the radical derives from the Bragg condition and the integration range is over real values. The first two terms of the radical correspond uniquely to the Eckart and Marsh régimes while the last term causes the low-frequency rolloff in the Rayleigh régime.

Equivalence of the two formulae is seen by changing the integration of Eq. 10A from wavenumber to angle variables θ' and ϕ as indicated in Ref. 8. From Eq. 9.3.10, $\Omega\, d\Omega$ becomes $k^2 \sin\theta' \cos\theta' d\theta'$ and, from Eqs. 9.6.1-3, $[\sin^2\theta + 2(\Omega/k)\cos\theta\cos\phi - (\Omega/k)^2]^{1/2} = \sin\theta'$.

Appendix B: Complex impedance

In Figure 11, tangential forces are assumed zero. For no losses, matching of horizontal wavenumbers at the ice/water interface gives the relations:

$$k\cos\theta = k_1\cos\beta = k_s\cos\eta$$

or: $\cos\beta = (c_1/c)\cos\theta \qquad \cos\eta = (c_s/c)\cos\theta$ 1B

Then: $\sin\beta = [1-(c_1/c)^2\cos^2\theta]^{1/2}$

$$\sin\eta = [1-(c_s/c)^2\cos^2\theta]^{1/2} \qquad 2B$$

The waves in ice become evanescent for imaginary values of the radicals. In evaluating the equation of Figure 11, we make use of the identities:

$$(\sin 2\eta)^2 = (2\sin\eta\cos\eta)^2 = 4\cos^2\eta(1-\cos^2\eta)$$

$$(\cos 2\eta)^2 = (2\cos\eta - 1)^2 \qquad 3B$$

The impedance equation is derived from Eq. 10.7 of Ref. 2 by taking the impedance of the air/ice interface to be zero. Note that the equation has been changed to $N^2 - M^2$ in place of $M^2 - N^2$ in order to correct for a change in sign of the arguments. That this is correct is seen from the asymptotic values $Z=i\,\rho_1 c_1\tan(k_1 D)$ at normal incidence and $Z\rightarrow i\,\rho_1\omega D$, $\omega\rightarrow 0$, where the latter is the mass-loading limit and $\rho_1 D$ is mass per unit area.

Losses are included by substituting $c_1(1+i\Delta_1)$ and $c_s(1+i\Delta_s)$. Values of Δ are both taken to be .02 for simplicity. The BASIC program for calculating Zi/Zo and Zr/Zo is shown in Figure 1B. The functions used in the subroutine are sinx/x and tanx/x, where x is the appropriate shear or compressional argument. The corresponding coefficients in the main program have been changed accordingly.

In all calculations, impedance is approximated as that of the unperturbed boundary. The method of Lapin [1B] is more general; however, resonance angles occur where the wavenumbers of the scattered field match the shear and compressional modes in the ice layer. Numerical solutions of the latter equations indicate that the errors are not serious, particularly at lower frequencies where impedance is nearly independent of angle.

Ref. 1B: A. D. Lapin, "Scattering of sound by a solid layer with rough boundaries", Sov. Phys. Acoust. 12 46-51 (1966)

```
'Ice impedance-Brekhovskikh
d0=4 ' ice thickness
cs=1800 'shear speed
cc=3000 'compressional speed
ds=.02 'loss tan shear
dc=ds 'loss tan compressional
rs=cs/1500:rc=cc/1500
xscale=3:yscale=1
GOSUB 1000 'Graphics
theta=8
t=theta/57.3:s=SIN(t):c=COS(t)
a0=2*(rs*c)^2
br=2*rs*a0*(1-3*ds^2) 'shear coefficients
bi=2*rs*a0*ds*(3-ds^2)
a1=a0*(1-ds^2)-1
ur=a1^2-4*a0^2*ds^2
ui=4*a0*a1*ds
a2=(rc*c)^2
u=1-a2*(1-dc^2)
v=-2*a2*dc
w=u^2+v^2
vr=(u+v*dc)/w
vi=(-v+u*dc)/w
ar=rc*(ur*vr-ui*vi) 'compressional coefficients
ai=rc*(ui*vr+vi*ur)
FOR n=0 TO 3 STEP .1
f=50*(n+1) 'acoustic frequency
k=2*3.14*f*d0/1500 'wavenumber*d0
r=rs:d=ds
GOSUB 2000
Msr=Mr:Msi=Mi:Nsr=Nr:Nsi=Ni
r=rc:d=dc
GOSUB 2000
Mcr=Mr:Mci=Mi:Ncr=Nr:Nci=Ni
Mr=ar*Mcr-ai*Mci+br*Msr-bi*Msi
Mi=ar*Mci+ai*Mcr+br*Msi+bi*Msr
Nr=ar*Ncr-ai*Nci+br*Nsr-bi*Nsi
Ni=ar*Nci+ai*Ncr+br*Nsi+bi*Nsr
zi=Mr-(Mr*(Nr^2-Ni^2)+2*Mi*Nr*Ni)/(Mr^2+Mi^2)
zr=Mi+(Mi*(Nr^2-Ni^2)-2*Mr*Nr*Ni)/(Mr^2+Mi^2)
zi=-zi*.9/k:zr=zr*.9/k        'normalize//Z0
x=x0+n*l
yi=y0-zi*h:yr=y0-zr*h
LINE (xt,ytr)-(x,yr):LINE (xt,yti)-(x,yi)
xt=x:ytr=yr:yti=yi
NEXT n
STOP
2000 'Subroutine
kkr=k/r/(1+d^2)
kki=-kkr*d
pp=1-(r*c)^2*(1-d^2)
qq=-2*d*(r*c)^2
w=(pp^2+qq^2)^(1/4)
ii=ATN(qq/pp)
IF pp>0 THEN 2100
ii=ii+3.141592654#
2100
sr=w*COS(ii/2)
si=w*SIN(ii/2)
kr=kkr*sr-kki*si
ki=kki*sr+kkr*si
cu=COS(kr)
su=SIN(kr)
jj=EXP(ki)
shu=(jj-1/jj)/2
chu=(jj+1/jj)/2
w=(su*chu)^2+(cu*shu)^2
ur=su*cu/w
ui=-shu*chu/w
vr=su*chu/w
vi=-cu*shu/w
Mr=ur*sr-ui*si
Mi=ur*si+ui*sr
Nr=vr*sr-vi*si
Ni=vr*si+vi*sr
RETURN
```

Figure 1B: BASIC program for Zi/Zo and Zr/Zo.

Appendix C: Impulse response

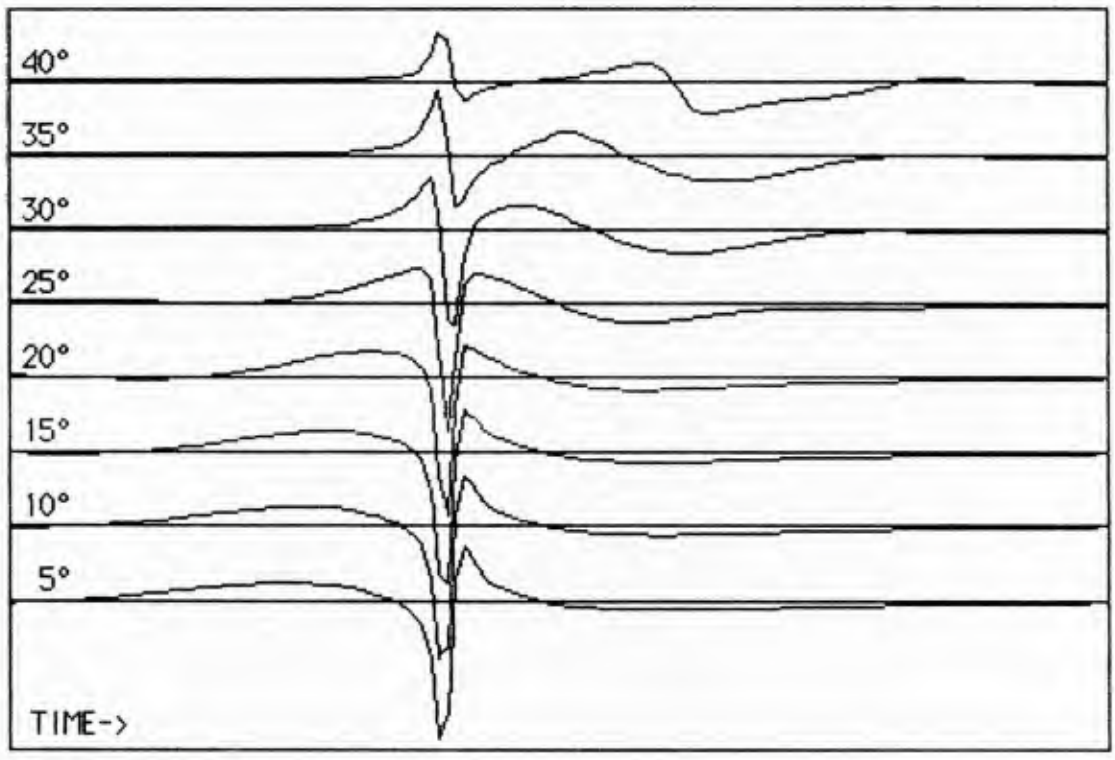

Figure 1C: Ice layer impulse response.

Figure 1C shows the impulse response of the ice layer as a function of grazing angle. The waveforms are calculated by inverse FFT (N=256) of the reflection coefficient Rz.

A gaussian waveform is used for the incident impulse (not shown), which is done by gaussian weighting the Fourier amplitudes. This serves to limit the peak amplitude and an also to prevent ringing at high frequency. The non-dimensional Fourier frequency of the fundamental is taken as FD=1. Overlap effects of adjacent periods appear negligible.

A time shift is needed in order to show the precursor properly. Instead of changing the impulse time, we take n=50 as the start time and make use of FFT periodicity.

The parameters used are the same as those in Figs. 12 and 13. The shear critical angle is roughly 33°. Individual reflections at both boundaries are seen at the larger grazing angles. The impulses merge at the critical angle where the shear wave becomes evanescent. Polarity of the high-frequency components then becomes negative. Inertial effects at lower frequencies and grazing angles is evidenced by the persisting slower oscillations.

Appendix D: Finite-impedance theory

Perturbation theory for both free and rigid surfaces is treated in Ref. 8. The respective boundary conditions are:

$$p+\zeta\,\partial p/\partial z=0$$

$$\partial p/\partial z+\zeta\,\partial^2 p/\partial z^2-\nabla p\cdot\nabla\zeta=0 \qquad 1D$$

where $\nabla=i\partial/\partial x+j\partial/\partial y$. In the rigid-boundary case, the slopes $\nabla\zeta$ involve horizontal-dipole reradiation while the displacements ζ involve vertical velocity-dipole reradiation analogous to a piston in a baffle. Equating the terms of the two perturbation orders to zero gives:

$$p_o=0 \qquad p_s+\zeta\,\partial p_o/\partial z=0$$

$$\partial p_o/\partial z=0 \qquad \partial p_s/\partial z+\zeta\,\partial^2 p_o/\partial z^2-\nabla p_o\cdot\nabla\zeta=0 \qquad 2D$$

Theory for finite-impedance boundaries is treated in Ref. 9. The analysis involves normal-modes and is of limited use in the plane-wave reflection case; however, the finite-impedance perturbation equation is given as:

$$p+\zeta\,\partial p/\partial z=(\partial p/\partial z+\zeta\,\partial^2 p/\partial z^2-\nabla p\cdot\nabla\zeta)\,(Z+\zeta\,\partial Z/\partial D) \qquad 3D$$

where $Z\approx Zi/\omega\rho$ (Zr can be neglected). Equations analogous to Eq. 2D become:

$$p_o-Z\partial p_o/\partial z=0$$

$$p_s-Z\partial p_s/\partial z=\zeta\,[(-1+\partial Z/\partial D)\partial p_o/\partial z+Z\partial^2 p_o/\partial z^2]-Z\nabla p_o\cdot\nabla\zeta \qquad 4D$$

The vertical-dipole component becomes:

$$p_s(1-ikZ\sin\theta')\approx\zeta\,(-1+\partial Z/\partial D)\,\partial p_o/\partial z=-\zeta\,[1-\partial Zi/\partial Zo]\,\partial p_o/\partial z \qquad 5D$$

which is the free-surface result with impedance correction factors. From the relations $kZ=Zi/\rho c$, $p_o=P_o(1+Rz)$, $\partial p_o/\partial z=ikP_o(1-Rz)\sin\theta$, the intensity coefficient for finite Z becomes:

$$Ro^2=[1-\partial Zi/\partial Zo]^2/\{[1+(\sin\theta'\,Zi'/\rho c)^2]\,[1+(\sin\theta\,Zi/\rho c)^2]\} \qquad 6D$$

which becomes a reflection factor in the free-surface integrand. Errors at lower frequencies are evidently not serious if we take $Zi'=Zi$.

The velocity-dipole term $Z(\partial p_s/\partial z+\zeta\partial^2 p_o/\partial z^2)$ is orthogonal and can be treated independently. By the same method, the solution for $Z=\infty$ is:

$$P_s^2(\theta',\phi)\approx P_o^2\,k^4\,A_o\sin^4\theta\,S_2(\Omega)/(\pi R)^2 \qquad 7D$$

where the element beam-pattern is now semi-isotropic. Averaged over a random ensemble of areas, the scatter-loss integral for finite Z becomes:

$$SL\approx 2\,k^4\sin^3\theta\int_0^{\pi/2}d\theta'\cos\theta'\,R\infty^2\int_{-\pi}^{\pi}d\phi\,S_2(\Omega)/\pi$$

$$=k^4\sin^3\theta\int_0^{\pi/2}d\theta'\cos\theta'\,R\infty^2\,S_1'(\Omega) \qquad 8D$$

where $R\infty^2=(\sin\theta'\,Zi'/\rho c)^2\,(\sin\theta\,Zi/\rho c)^2/\{[1+(\sin\theta'\,Zi'/\rho c)^2][1+(\sin\theta\,Zi/\rho c)^2]\}$ is the effective reflection factor.

By the same method, the horizontal-dipole solution for $Z=\infty$ is:

$$P_s^2(\theta',\phi) \approx P_0^2 k^2 A_0 \cos^2\theta \, \Omega_x^2 S_2(\Omega)/(\pi R)^2 \qquad 9D$$

where $\Omega_x = k(\cos\theta - \cos\theta'\cos\phi)$ is the Bragg condition associated with the gradient of ζ.

Results are quite different from the vertical-dipole case. At the lower frequencies, most of the scatter is backwards. Forward scatter increases with increasing frequency and backscatter decreases. The element beam pattern is not the usual horizontal-dipole pattern because the excitation phase is delayed along the x axis and the dipole null occurs in a semi-cone ($\Omega_x = 0$) including the specular direction.

Averaged as in Appendix A, the scatter-loss integral for the horizontal-dipole component with finite Z is:

$$SL \approx 2 k^2 \cos\theta \cot\theta \int_0^{\pi/2} d\theta' \cos\theta' R_\infty^2 \int_{-\pi}^{\pi} d\phi \, \Omega_x^2 S_2(\Omega)/\pi \qquad 10D$$

Assuming no coherence between slopes and displacements, this component is independent and additive also.

Equivalent equations for the velocity and horizontal-dipole components can also be derived by the method of B&L [8]. For $Z=\infty$ the equation for the velocity-dipole component is:

$$SL \approx 2 k^2 \sin^3\theta \int_\Omega d\Omega \int d\phi \, S_2(\Omega)/\pi \sin\theta' \qquad 11D$$

and the equation for the horizontal-dipole component is:

$$SL \approx 2 \cos\theta \cot\theta \int \Omega^3 d\Omega \int d\phi \cos^2\phi \, S_2(\Omega)/\pi \sin\theta' \qquad 12D$$

where $\sin\theta' = [\sin^2\theta + 2(\Omega/k)\cos\theta\cos\phi - (\Omega/k)^2]^{1/2}$ and the range of integration is over real values of the radical.

The rigid-boundary case is also treated in Ref. 1D by a different method. The asymptote in the Eckart régime is shown to be $SL = (2kh\sin\theta)^2$, which is the same (magnitude) as the free-surface case. This result is obtained from Eq. 11D, keeping only the first term in the radical. The asymptote in the Marsh régime is $SL \propto (kh)^2/(kL)^{3/2} \sin\theta$. This result is obtained from Eq. 12D, keeping only the second term in the radical. The asymptote in the Rayleigh régime is $SL \propto \cos\theta \cot\theta (kh)^2/(kL)$. This result is also obtained from Eq. 12D by including the third term in the radical. Numerical results of Eqs. 8D and 10D for $Z_i=\infty$ have been found to be identical.

Ref. 1D: Y. P. Lysanov, "Scattering of Sound by Irregular Surfaces", in Ocean Acoustics ed. L. M. Brekhovskikh (Moscow, 1974) Part IV.

TR 8089

INITIAL DISTRIBUTION LIST

Addressee	No. of Copies
CINCLANTFLT	1
CINPACFLT	1
SUBMARINE GROUP 2	1
SUBMARINE GROUP 5	1
SUBMARINE GROUP 6	1
SUBMARINE GROUP 7	1
SUBMARINE GROUP 8	1
SUBMARINE GROUP 9	1
SEC NAV	1
DIA	1
DTIC	1
DARPA	1
NOP-095	1
NOP-952	2
NOP-098	1
NOP-02	1
OCNR-00	1
OCNR-10	1
OCNR-122	1
OCNR-13	1
OCNR-20	1
ONR DET BAY ST. LOUIS	1
ONR DET BOSTON	1
ONR DET PASADENA	1
SPAWAR-05	2
NAVSEA (PMS-402)	1
NRL	1
NORDA	1
NCSC	1
NOSC	1
NOSC DETACHMENT HAWAII	1
NUSC (00, 01)	2
NUSC NEW LONDON LAB (60, 61, 61M, 33, 33A, 21)	6
NUSC NEWPORT LAB	4
NAVAL OCEANOGRAPHY COMMAND	1
NAVAL OCEANOGRAPHIC OFFICE	1
FLEET NUMERICAL OCEANOGRAPHY CTR	1
NTSA	1
NPS	1
NWC	1
SUBMARINE SCHOOL (Code 40, 20)	2
WOODS HOLE OCEANOGRAPHIC INSTITUTION (Watkins)	1
UNIV OF CT, AVERY POINT (Bohlen, Marine Sci. Dept.)	1
UNIV OF CT, STORRS, CT (Bennett, Mech. Engr. Dept.)	2